Enhanced charge transport and photovoltaic performance induced by incorporating rare-earth phosphor in organic/inorganic hybrid solar cells

Zihan Chen[1,§], Qinghua Li[1,§,*], Chuyang Chen[2], Jiaxing Du[3], Jifeng Tong[3], Xiao Jin[1], Yue Li[1], Yongbiao Yuan[1], Yuancheng Qin[1], Taihuei Wei[4,*], Weifu Sun[2,*]

[1]Key Laboratory of Nondestructive Testing，Ministry of Education, Nanchang Hangkong University, Nanchang, 330063, P. R. China

[2]School of Materials Science and Engineering, The University of New South Wales, Sydney, NSW 2052, Australia

[3]Institute of the Ministry of Science Research, Academy of Armored Force Engineering, Beijing, 100072, P. R. China

[4]Department of Physics, National Chung-Cheng University, Chia-Yi 621, Taiwan, Republic of China

*Corresponding author: E-mail address: qhli@hqu.edu.cn, Tel.: +86 791 8645 3203, Fax: +86 791 8645 3203; twei@ccu.edu.tw; weifu.sun518@gmail.com.

§These authors contributed equally.

Abstract: In this work, dysprosium ion decorated yttrium oxide (Dy^{3+}:Y_2O_3) nanocrystal phosphors was incorporated into TiO_2 acceptor thin film in a bid to enhance the light harvest, charge separation and transfer in the hybrid solar cells. The results show that the energy level offset between the donor (P3HT) and the acceptor (Dy^{3+}:Y_2O_3-TiO_2) has been narrowed down, thus leading to the enhanced electron and hole transports, and also photovoltaic performances as compared to pure TiO_2 without incorporating Dy^{3+}:Y_2O_3. By applying femtosecond transient optical spectroscopy, after the incorporation of dopant Dy^{3+}:Y_2O_3 into TiO_2 at 6wt%, both the hot electron and hole transfer lifetimes have been shortened, that is, from 30.2 ps and 6.94 ns to

25.1 ps and 1.26 ns, respectively, and an enhanced efficiency of approaching 3% was achieved as compared to 2.0% without doping, indicating that the energetic charges are captured more efficiently and hence benefits a higher power conversion efficiency. Moreover, the results reveal that both the conduction band (CB) and valence band (VB) edges of the acceptor were elevated by 0.57 and 0.32 eV, respectively, after incorporating 6 wt% $Dy^{3+}:Y_2O_3$. This work demonstrates that distinct energy level alignment engineered by $Dy^{3+}:Y_2O_3$ phosphor has an important role in pursuing efficient future solar cells and underscores the promising potential of rare-earth phosphor in solar applications.

Keywords: Nanoparticle, phosphor, doping effect, charge transport dynamics, hybrid solar cells

1. Introduction

Hybrid solar cells (HSCs) based on inorganic semiconductors (e.g., nanocrystal titanium dioxide TiO_2) and organic materials (*e.g.*, poly(3-hexylthiophene), P3HT), have drawn intensive attention due to the potentials of combining the advantageous properties of the two types of materials, such as the highly delocalized electronic states and the significant dielectric constant of inorganic semiconductors, or the low-cost of the solution-processing of polymer.[1-10] Over the last five years, most of the reported power conversion efficiency (PCE) of organic/inorganic hybrid bulk-heterojunction (BHJ) solar cells based on the well-known conducting polymer P3HT is around 2%, ranging from 1.0~3.0%. [11-13] However, note that much higher PCE of above 5% has been achieved for polymer solar cells based on P3HT by device optimization or molecular design of new electron acceptor.[14,15] Since the solution-processed photovoltaic devices typically suffer from the low efficiency. One of the promising approaches to enhance the device performance is the effective energy level alignment to narrow the energy offset and hence promote the charge carrier transfer at the interface of the BHJs. It is known that the energy offset between the lowest unoccupied molecular orbit (LUMO) levels of P3HT donor andTiO_2 acceptor is about 1.2 eV and this energy offset at the donor/acceptor interface is sufficient to break the Coulomb attraction (typically 0.1~0.5eV) but not in an efficient way [16,17]. However, because of the initial cooling process, a substantial amount of solar energy has already been irreversibly lost [18,19]. Besides, it is well-established that the open circuit voltage is dependent on the energy band positions of acceptor and donors [20-22]. Therefore, it would not only benefit charge transport but also favor the enhancement of open circuit voltage if an appropriate energy offset at the interface of the donor and acceptor could be engineered by utilizing the doping of foreign ions or compounds into the acceptor colloid by the low-cost solution-processing.

Recently, much effort has been devoted to the photoluminescence of the rear-earth ion doped semiconductor materials to broaden the absorption domain for solar cell applications [23-27], especially the down-conversion of ultraviolet light to visible light [27]. The typical way to achieve the photoluminescence is via an energy transfer using rare-earth ions (e.g., Dy^{3+}) owning to their unique and rich energy level structure [28,29], allowing for efficient spectral modification. These nanometer-sized inorganic materials can exhibit a wide range of optical and electrical properties[30]. A host-guest hybrid material with novel properties would be obtained by incorporating foreign ions or compound into the host material. Dy^{3+} is one of the most efficient rare earth (RE) ions, owing to its versatile energy levels in the near ultraviolet region and the effective energy transitions in an appropriate host material. On the other hand, yttrium oxide (Y_2O_3) is one of the most promising down-converted host materials for rare earth ions because of the similarities in the chemical properties and the ionic radii of rare earth ions of Dy^{3+} and Y^{3+}. Moreover, Y_2O_3 possesses good phase stability, low thermal expansion and wide transparency range (from ultraviolet to mid-infrared), and also has a low phonon energy that is essential for efficient photoluminescence by minimizing energy loss.[31,32] Herein, the Dy^{3+}ion-decorated yttrium oxide (Y_2O_3) will be incorporated into TiO_2 acceptor. The intensively pursued nanocrystalline rare-earth phosphors, which can broaden the absorption domain to enhance the exciton generation and improve the transfer of charges by the doping effects have attracted significant attention due to their intrinsic and unique conversion properties [33]. Especially, europium or yttrium ion has demonstrated an excellemt enchancement of ultraviolet light harvesting via a down-conversion luminescence process in DSSC devices [34-36]. However, seldom evidence has been provide to substantiate the control of energy band position originating from rare-earth phosphor dopant and the charge photogeneration dynamics in HSCs has rarely been reported. Herein, we focus on the intensively pursued doping effects of nanocrystalline rare-earth phosphor dopant to broaden the absorption domain and engineer energy level alignment of the BHJ, and eventually to enhance the exciton dissociation and charge transport in HSCs.

2. Experimental

2.1 Materials

All analytical purity chemical reagents including tetrabutyl titanate, poly(ethylene glycol) (PEG, molecular weight of 20000), nitric acid, sodium hydrate, P25(Degussa), OP emulsifying agent (Triton X-100), tetrabutylammoniumhexafluorophosphate ($TBAPF_6$), acetonitrile, isopropanol, yttrium oxide, didysprosium trioxide, conjugated polymer P3HT and poly(3,4-ethylenedioxylenethiophene) polystylene sulfonic acid (PEDOT:PSS) were purchased from Sigma-Aldrich Ltd., Hongkong, China except otherwise indicated. Fluorine-doped tin oxide glass (FTO, sheet resistance 8 Ω cm^{-2}) was purchased from Hartford Glass Co., USA.

2.2 Preparation of Dy^{3+}:Y_2O_3 phosphor

Dy^{3+}:Y_2O_3 phosphors were prepared by a minor modification of the hydrothermal method according to the following procedures[25,26]. Firstly, Y_2O_3 (0.040 mol) and Dy_2O_3 (0.002 mol) were mixed and homogenized thoroughly. Then, adequate nitric acid was added into the mixture under heating and stirring. After being completely dissolved, the mixture was quickly transferred into a Teflon-lined stainless-steel autoclave. Then, the compounds were dissolved in deionized water, and then a 10 M NaOH solution was added dropwise under stirring. Afterwards, an appropriate amount of de-ionized water was added until the filled degree reached 80% of the total container volume. The obtained solution was hydrothermally treated at 200 ^{o}C for 12

h. After being naturally cooled to room temperature, the obtained product was centrifuged, washed until the pH value of the system equaled to 7, and then dried in air at ambient temperature, followed by sintering in air at 850 ºC for 30 min. Finally, Dy^{3+}:Y_2O_3 phosphors were obtained.

2.3 Synthesis of Colloidal nanocrystalline rare-earth phosphate doped TiO_2

The rare-earth phosphor doped TiO_2 colloid was prepared by the following procedure in a similar way as reported[37,38]. Tetrabutyl titanate (10 mL) was added to 100 mL of distilled water under stirring, and then a white precipitate was produced immediately. The precipitate was filtered using a glass frit and washed with distilled water. The filter cake was then transferred to a mixed solution (150 mL) contained 1 mL nitric acid and 10mL acetic acid at 80 °C, under vigorous stirring a light blue TiO_2 precursor was formed. Followed by an ultrasonic stirring for 30 min, the mixture was hydrothermally treated in an autoclave at 200 °C for 24 h to form a colloid of TiO_2. Then the 1 wt% P25 and a certain amount of Dy^{3+}:Y_2O_3 phosphors were added into TiO_2 colloid by repeating crystallization at 200 °C for 12 h. Finally the resultant slurry was concentrated to 1/5 of its original volume by a thermal evaporation, and then 0.5 g PEG-20000 and a few drops of the Triton X-100 emulsification reagent were added to produce an even and stable TiO_2 colloid.

2.4 HSCs device fabrication

A layer of nanocrystalline rare-earth phosphor doped TiO_2 acceptor film with a thickness of 200 nm was prepared by coating the TiO_2 colloid on FTO glass using a doctor blade technique, followed by sintering in air at 450ºC for 30 min. Since the electron transfer process was more efficient if the donor was adsorbed on the acceptor [39]. Thus, the acceptor film was soaked in a 0.15 mmol/mL conjugated polymer P3HT toluene solution for 12 h to uptake P3HT molecules for the fabrication of BHJ. Then, the PEDOT:PSS layer was spin-coated onto the BHJ. Finally, Pt electrodes were deposited on the top of the PEDOT:PSS layer as counter electrode by thermal evaporation under vacuum.

2.5 Characterizations

The phases of the prepared powders were identified by a Rigaku MiniFlex II X-ray diffractometer (XRD) using Cu Kα radiation (λ = 0.154 nm) at a power of 30 kV and 40 mA. The XRD patterns were collected in a scan mode at a scanning speed of 5°·min^{-1} in the 2θ range between 10 and 70°; The microstructure of the Dy^{3+}:Y_2O_3 phosphor was characterized by using a transmission electron microscope (TEM, JEM-2010, JEOL Ltd.) and high resolution (HR)-TEM and selected area electron diffraction (SAED) patterns working at 200 kV. Samples for TEM and HR-TEM characterizations were prepared by ultrasonically dispersing the samples in absolute ethanol, placing a small volume of this suspension on carbon-enhanced copper grids, and then drying in air. Energy dispersive X-ray spectroscopy (EDS) data were recorded by using a field emission scanning electron microscopy (FE–SEM, Hitachi S3500N) equipped with an EDS detector (OXFORD 7021). The cyclic voltammetry (CV) results were obtained using a BAS 100B instrument at room temperature at a scan rate of 50 mV s^{-1} with 0.1 M $TBAPF_6$ in acetonitrile as the supporting electrolyte, a platinized platinum ($0.5 cm^2$) as the counter electrodes and Ag/Ag^+ electrode as the reference electrode. The values are expressed in potentials versus Fc/Fc^+. The TiO_2, $Dy^{3+}:Y_2O_3$ doped TiO_2 and $Dy^{3+}:Y_2O_3$ films are used as work electrodes, respectively. Mott-Schottky measurements were done at the frequency of 1 kHz in the aqueous solution of 0.05 M Na_2SO_4 using a BAS 100B instrument and Ag/Ag+ electrode as the reference electrode. The photoluminescence (PL) spectrum was measured by using a spectrophotometer (FLS920, Edinburgh), in which a xenon lamp and a photomultiplier tube (R955, Hamamatsu) were used as excitation source and fluorescence detector, respectively. The incident photon-to-current conversion efficiency (IPCE, also termed as external quantum efficiency) measurements were performed at short-circuit condition. A class A quality solar simulator (PEC-L11, AM1.5G, Peccell Technologies, Inc., Kanagawa, Japan) served as a light source. The light was directed through a monochromator (model 74100, Oriel Instrument, California, USA) onto the HSCs. The photocurrent-voltage (*J*-*V*) curves of the assembled HSCs were recorded on an Electrochemical Workstation (Xe Lamp Oriel Sol_3A™ Class AAA Solar Simulators 94023A，USA) under the irradiation of a simulated solar light from a 100 W xenon arc lamp in ambient atmosphere.

2.6 Electron/hole transport primary dynamic

The ultrafast light source with a temporal resolution of ~120 fs was generated by a mode-locked titanium-sapphire laser operating at 800 nm. An optical parametric amplifier (OPA-800CF-1, Spectra Physics) provided ultra-short laser pulses at desired wavelengths (~120 fs, full width at half maximum). A continuum white light generated from a sapphire plate was directed into the excited sample and detected by a charge coupled device (CCD) detector. Ultra-short laser pulses at 400 nm were employed as the pump light for the sample excitation and the probe light for the absorption measurement. Transient absorption at various delay times could be measured by controlling the arrival time of each laser pulse at the sample.

3. Results and discussion

3.1. Characterizations of the prepared powder

The XRD pattern of the prepared powders Dy^{3+}:Y_2O_3 nanophosphors is shown in **Fig. 1**a. It reveals that all the diffraction peaks can be readily indexed as those of cubic yttrium oxide Y_2O_3. In detail, the peaks at 21.645°, 29.125°, 33.307°, 48.318° and 57.362° obtained from XRD pattern are in excellent with those of Y_2O_3 according to JCPDS 86-1107, corresponding to 20.5006°, 29.1523°, 33.7871°, 48.5351° and 57.6246°, respectively. It is worth mentioning that both Y^{3+} and Dy^{3+} ions have similar electronic structure as well as similar ionic radii of these atoms (Y=0.9 Å, Dy=0.912 Å), which favors the successful replacement of Y^{3+} ions with Dy^{3+} ions. Meanwhile, Y_2O_3 and Dy_2O_3 were completely dissolved and mixed during the course of the hydrothermal preparation. Therefore, although the initial loading amount of Dy^{3+} is as small as 5 mol% only relative to Y_2O_3, nevertheless Dy^{3+} can enter Y_2O_3 lattice to form the so-called Dy^{3+} decorated Y_2O_3. Besides, as shown in Fig. 1a, the individual characteristic peaks of bare TiO_2 and Y_2O_3 can be clearly demonstrated, and those peaks also are clearly reflected in Dy^{3+}:Y_2O_3-doped TiO_2 film. Fig. 1b shows the TEM image of the dysprosium ion decorated yttrium oxide nanophosphors, that is, Dy^{3+}:Y_2O_3, most of which are in the order of about 100 nm in diameter and still within nano-domain. Fig. 1c and 1d reveal the HR-TEM images and the corresponding SAED patterns of Dy^{3+}:Y_2O_3 nanophosphors. The estimated distance spacing of d_1=0.546 nm, d_2=0.433 nm estimated from the HR-TEM images are in agreement with those from the standard XRD pattern, i.e., d_1=0.5301 nm, d_2=0.4328 nm, which lend further support to the above XRD analysis.

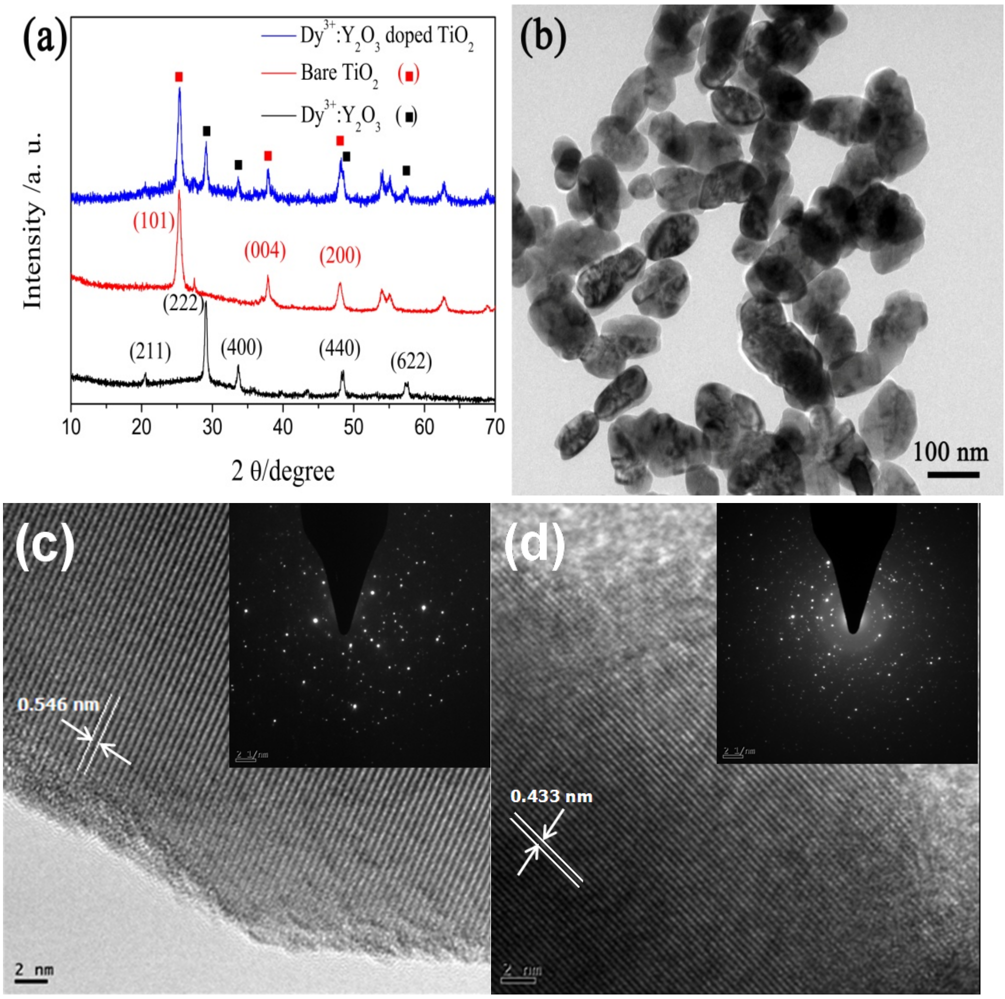

Fig. 1. (a) XRD patterns of bare TiO_2, dysprosium ion decorated yttrium oxide (Dy^{3+}:Y_2O_3) and Dy^{3+}:Y_2O_3-doped TiO_2; (b) TEM images of the prepared Dy^{3+}:Y_2O_3; (c) and (d) HR-TEM images showing an individual nanocrystal of Dy^{3+}:Y_2O_3 and the

insets are the corresponding SAED patterns.

3.2. Energy Level engineering by doping Dy^{3+}:Y_2O_3

An efficient solar device not only requires the wide adsorption of solar spectrum, but also an excellent separation of the photogenerated electron-hole pairs into long-lived dissociated charges with a high quantum yield and minimal loss of free energy[40-42]. Herein, the role of rare earth ion Dy^{3+} acts as down-conversion to broaden the absorption of solar spectrum (Fig. S1, Electronic Supporting Information) and the optimal initial molar loading of Dy^{3+} relative to Y_2O_3 was optimized and determined to be 5mol% as shown in Fig. S2, Electronic Supporting Information. One route for highly efficient charge transfer needs to compress the geminate recombination of electron-hole pairs and to gain a long diffusion length and also requires quick extraction of electrons and holes. Consequently, in order to achieve a higher efficiency, after rare-earth phosphor was doped, the present work turns to investigate the effects of the energy band control induced by Dy^{3+}:Y_2O_3 phosphor and its influences on the charge transport dynamics. The primary dynamics investigation helps to disclose the innate dynamics of the photoexcited charges in P3HT and the photogenerated electron-hole transfer at the interface of donor and acceptor in HSCs. Not that as will be discussed in Fig. 5d, the optimal loading of Dy^{3+}:Y_2O_3 phosphor in acceptor TiO2 film is about 6 wt%, because it becomes hard to form a flat acceptor film when exceeding 6 wt%; on the other hand, with further increasing the loading, the elevation of CB energy level does not change much and only improve slightly

(Table S2). Therefore, the studies on the photogeneration dynamics were based on the doping of $Dy^{3+}:Y_2O_3$ at 6wt%. Herein, through femtosecond transient absorption spectroscopy (TAS) of organic/inorganic BHJs with selective probe wavelengths, we have successfully monitored electron, hole transfer (~ps) and the dynamics of electron-hole recombination (~ns) as shown in Figure 2 and evidenced that both the charge transfer time and the efficiency are enhanced by doping with $Dy^{3+}:Y_2O_3$ phosphors.

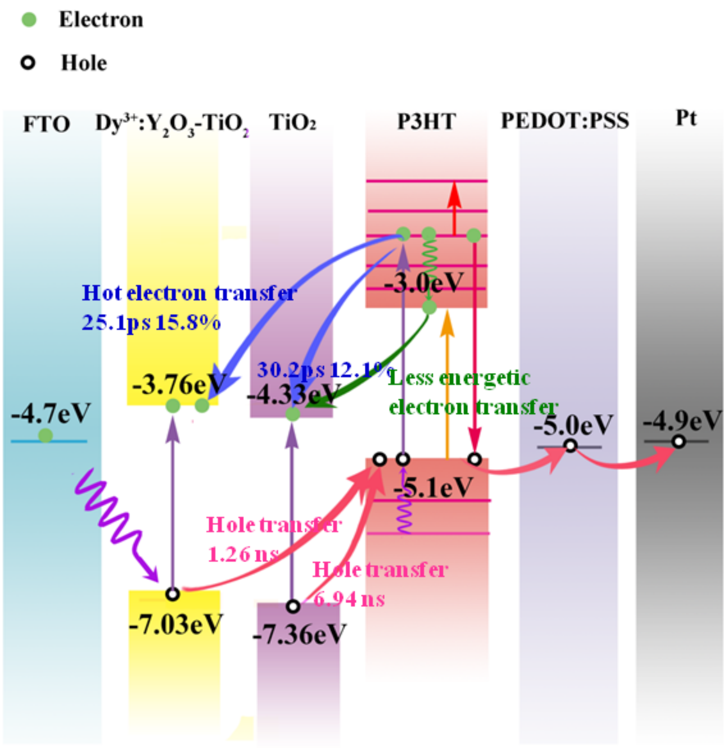

Fig. 2. Energy level diagram of acceptor/donor showing optical excitation (up arrow), nonradiative relaxation (curved line), radiative relaxation (down arrow) and the electron and hole transfer times at the either $Dy^{3+}:Y_2O_3$ doped TiO_2/P3HT or TiO_2/P3HT interfaces. $\left|n\right\rangle$ refers to the vibrational eigenstates involved in the transitions. The VB and CB energy levels of pure TiO_2 are also shown for comparison. The LUMO and HOMO of P3HT are -3.0 and -5.1 eV, respectively.

The conduction band (CB) level of electro-extraction layer (e.g., Dy^{3+}:Y_2O_3-TiO_2) is below than that the lowest unoccupied molecular orbit (LUMO) level of P3HT, whereas the energy level of hole-extraction layers (PEDOT:PSS) is above than the highest occupied molecular orbit (HOMO) level of P3HT, thus enabling the delocalized electrons to diffuse towards a donor/acceptor interface while the hole to transfer to the hole-extraction layer (i.e., PEDOT:PSS) as illustrated in Fig. 2. Energy-band model shown in Fig. 2 was used to interpret the charge photogeneration, transfer and the subsequent relaxation. At the thermal equilibrium, the unperturbed P3HT molecules reside in the ground state S_0. Under the excitation of 400-nm laser pulse, electrons are promoted to the vibronic levels of excited state $S_1|n\rangle$ in P3HT molecules, and then the holes are formed in the ground state S_0, that is, the so-called charge delocalization (generation). Then the delocalized electrons undergo one of the following three processes: (a) recombination with the holes in the ground state with a decay time constant of τ_{re}; (b) relaxing to the lower vibronic level of excited state S_1 with a decay time of τ_{vib1} (within ~1ps) [43]; c) transfer to the interface of BHJ.

An efficient energy conversion in HSCs requires quick extraction of those hot charges before they cool down. Next, we will prove that the favorable energy level alignment can be obtained by doping Dy^{3+}:Y_2O_3 phosphors, which results in the enhancements of both the electron and hole transfers. Therefore, the hot charge transfer becomes more competitive than cooling process.

3.3. Electron transfer dynamics

Transient absorption spectra of donor/acceptor films measured from 1 to 900 ps are shown in Fig. S4. Note that the negative long-lived absorption bands at 602 nm are ascribed to the photobleaching (PB) of the ground state absorption (S0, S1) of P3HT, which is consistent with the ultraviolet-visible absorption peak (Fig. S3). The absorption peak at ~650 nm is observed immediately after the laser excitation and is ascribed to photoinduced excited states absorption (PA). For 400-nm photoexcitation, it is reasonable to attribute the 650-nm PA band to state-filling effects [44,45].

The transient absorption dynamics probed at 650 nm are shown in Fig. 3. The complex state-filling effects can be regarded as the excited state absorption from S_1 $|n\rangle$ to the higher levels with an absorption cross section $\sigma_{S1} > \sigma_{S0}$. Thus, the transient photoinduced excited states absorption (PA) decay monitors the variation of the delocalized electron population of the excited state $S_1|n\rangle$ in P3HT. The TAS signals for both the TiO_2/P3HT and Dy^{3+}:Y_2O_3 doped TiO_2/P3HT films in Fig. 3 have prominent contributions from the electronic hyperpolarizability near zero delay, but exhibit a complicated temporal profile at positive time delay. We have decomposed the TAS signals of these films into four dynamically distinct components that appear to the organic/inorganic blend films[45,46]. These components include: 1) an instantaneous response of the electronic contribution that is represented by a scalar multiple of the cross-correlation function between the pump and probe pulses; 2) a fast component (< 1 ps) that accounts for the prominent shoulder in the upper curves; 3) an intermediate component with an exponential decay in the range 1-50 ps; 4) and a most slow component, which accounts for the TAS at the longer time delay (> 50 ps). Thus, $\phi(t)$ can be described with a superposition of contributions:

$$\phi(\mathrm{t}) = \delta(\mathrm{t}) + \mathrm{A}\exp(-\mathrm{t}/\tau_{\mathrm{vib1}}) + \mathrm{B}\exp(-\mathrm{t}/\tau_{\mathrm{hot\text{-}e}}) + \mathrm{C}\exp(-\mathrm{t}/\tau_{\mathrm{re}}) \tag{2}$$

where δ(t) is the purely electronic hyperpolarizability that responses instantaneously to the applied laser field (Fig. 3 PA1), the second term is the nonradiatively decay of vibronic relaxation $|n\rangle \rightarrow |0\rangle$ in P3HT after the excitation by the pump pulses (Fig. 3 PA2), the third term is the hot electron transfer to the interface of the heterojunction contributions to the detected signal with a transfer time of $\tau_{\text{hot-e}}$ (Fig. 3 PA3), and the last term is the contribution of the recombination of the electron-hole pairs with a time constant of τ_{re}, respectively (Fig. 3 PA4). All these decay transients are well fitted with a three exponential decays with nonlinear least squares fitting of the whole delay time and all the constants are listed in Table 1. The efficiency of hot electron transfer can be estimated by using the ratio of the amplitude B/(A+B+C). For pure TiO_2/P3HT and Dy^{3+}:Y_2O_3 doped TiO_2/P3HT, the hot electron transfer time and the efficient are $\tau_{\text{hot-e}}$=25.1 ps, 15.8% and $\tau_{\text{hot-e}}$=30.2 ps, 12.1%, respectively. It is evident that with Dy^{3+}:Y_2O_3 doped TiO_2 as acceptor layer present, the hot electron transfer lifetime becomes shorter, and the transfer efficient becomes higher as compared to pure TiO_2. All these outcomes can be ascribed to the energy level alignment of acceptor induced by the Dy^{3+}:Y_2O_3 phosphors. That is, the CB and VB positions of TiO_2 are elevated by 0.57 and 0.32 eV, respectively. Correspondingly, the energy offset between LUMO energy level of the donor and the CB of the acceptor is narrowed from 1.33 to 0.76 eV; meanwhile, the energy offset between HOMO energy level and the VB of acceptor decreases from -2.26 to -1.94 eV, as shown in Table S1. It is worth mentioning that the results obtained in this work should be reliable. On one hand, as observed from TA spectra, a prominent symmetrical peak that accounts for approximately 90% of the peak amplitude is clearly observed near zero delay, immediately followed by a fast decay in the time domain 1~5 ps. Subsequently, an intermediate component in the range of 1~30 ps was clearly observed. Finally, a long tail dominates the contribution in long time delay. This concept was detailed by the highly-cited work done by D. McMorrow, et al.,[47] and the method of least-squares deconvolution (LSD) was employed to obtain the parameters by fitting the TA spectra, which has gained recognition and widely been used.[48-50] On the other hand, TAS measurements were carefully carried out to obtain reliable results. The laser system was operated at a repetition rate of 10 Hz, and the corresponding time interval of each pulse is 0.1 s. Since the time interval was long enough for the sample to reach fully thermodynamic equilibrium before the next pulse arrived, thus the already fully relaxed sample can be excited by each pulse. Each data was obtained by averaging 100 individual measurements to improve the signal-to-noise ratio, and the typical detection sensitivity of the difference absorption (ΔOD) was better than 10^{-4}.

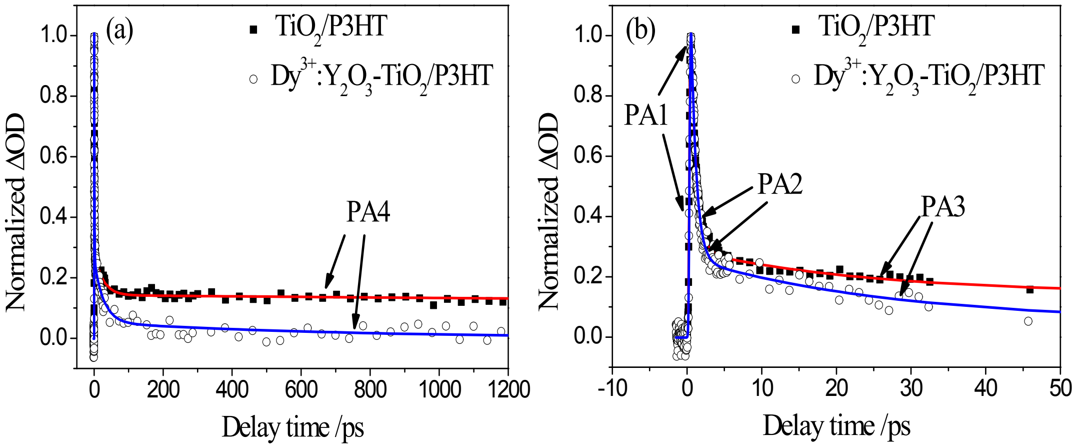

Fig. 3. (a) Normalized femtosecond transient absorption decays of Dy^{3+}:Y_2O_3 doped

TiO_2/P3HT (○) and pure TiO_2/P3HT (■) films excited at 400 nm (100 μJ cm^{-2}) probed at 650 nm. Solid lines are fitting curves with exponential components. (b) The early time dynamics probed at 650 nm.

For Dy^{3+}:Y_2O_3-TiO_2 and pure TiO_2, the electron-hole recombination times were obtained to be τ_{re}=0.7 and 14.0 ns respectively, indicating that with Dy^{3+}:Y_2O_3 doped TiO_2 as acceptor layer present, the delocalized electrons decay much faster than pure TiO_2. However, from the transient absorption dynamics of PB (Fig. 4), there is no restoration of the hole in the valence band in P3HT on the long time scale (50 ps to 1.2 ns) with either pure TiO_2 or Dy^{3+}:Y_2O_3 doped TiO_2 as acceptor present. If all the electrons that depart from the S_1 state relax to the ground state S_0, the hole population decay should resemble the PA signal. On the basis of conservation of particle number, the discrepancy of the electron-hole recombination time and the hole decay time can be attributed to the 'less energetic' electron transfer from donor to acceptor. In other words, there exists another pathway for electron relaxation. In fact, those hot electrons in a vibronic energy level of $S_1|n\rangle$ state first relax to a lower vibronic energy level $S_1|0\rangle$, and then may have enough time to transfer from donor to acceptor because of the long geminate recombination time (~ns). As the initial cooling process, a lot of energy dissipates by emission of phonons, and then those hot electrons develop into less energetic electrons. Moreover, the less energetic electron transfer time can be estimated on the order of ns due to the decay time quenching from 14.0 to 0.7 ns. Therefore, the reduction of the electron-hole recombination time represents a large number of less energetic electrons transfer to the interface. Thus, we conclude that through optimizing the energy level configuration induced by Dy^{3+}:Y_2O_3 phosphor not only reduces the hot-electron transfer time, but also improves the less energetic electrons transfer.

3.4. Hole transfer dynamics

Since the transient PB decay monitors the variation of hole population of the ground in P3HT. The transient absorption decays probed at 602 nm are performed as shown in Fig. 4 to investigate the hole transfer dynamics. Particularly, after being excited by femtosecond laser pulse of 400-nm (about 3.1 eV), which is greater than the band gaps of both donor (~3.0 eV) and acceptor (~2.1 eV) molecules, thus both P3HT and TiO_2 were promoted to the excited states, and a large number of holes were formed in the valence band of acceptor and donor while many electrons were created in the conduction band. The hole decays in the ground state of P3HT experienced three competitions: the hole transfer from acceptor to P3HT, the recombination with the electrons in excited state S_1 and the hot hole cooling from the lower vibrational relaxation. The hole transfer from acceptor to donor gives rise to the hole population, while both the cooling of hot holes and the recombination with electrons reduce the population of holes. There exists a competition between the generation of new holes and the quenching. However, the photobleaching dynamics reveal that the population of hole increases in the time domain (from 100 ps to 1.2 ns) despite the recombination of the electron-hole pairs, indicating that the hole transfer is dominant in the long time scale. Nevertheless, early time decays originating from the vibronic relaxation of holes occurred quickly, typically in several sub-picoseconds. Therefore, the transient photobleaching of the ground state absorption decays can be described with a sum of two exponential functions:

$$\phi(\mathrm{t}) = \delta(\mathrm{t}) + \mathrm{D}\exp(-\mathrm{t}/\tau_{\mathrm{vib2}}) + \mathrm{E}\exp(\mathrm{t}/\tau_{\mathrm{complex}}) \tag{3}$$

where the second term is the nonradiatively decay from lower vibronic level inducing the hot-hole cooling (Fig. 4 PB2), the third term represents the complex contributions to the detected signal: the hole transport with a hole transfer lifetime τ_h and the recombination of the electron-hole pairs $S_1|n\rangle \rightarrow S_0$ (n=1, 2, 3…) with an effective fluorescence decay time constant τ_{flu} (Fig. 4 PB3). There exists a competition between the generation of new holes and the quenching, thus the hole transfer time τ_h can be estimated by using the relation $1/\tau_{complex}=1/\tau_h-1/\tau_{flu}$ [51], in which τ_{flu} was estimated to be about τ_{flu} =38±12 ns [52]. From fitting the normalized absorption decays by Eqs (1) and (3), with either Dy^{3+}:Y_2O_3 doped TiO_2 or pure TiO_2 layer (electron acceptor) present, we found that the corresponding hole transfer time decreases to 1.26 from 6.94 ns. This phenomenon can be well interpreted by the Marcus theory: in the “inverted” region, the electron transfer rate increases with decreasing the energy offset between the conduction bands acceptor and donor. In current case, after doping Dy^{3+}:Y_2O_3, the energy offset between the VB edge of acceptor and HOMO energy level of donor is narrowed down from 2.26 to 1.94 eV and should fall within the “inverted” region herein. The narrowing of energy offset causes the hole transfer to the interface in a more efficient way with less energy loss, thus in turn boosting charge separation in HSCs.

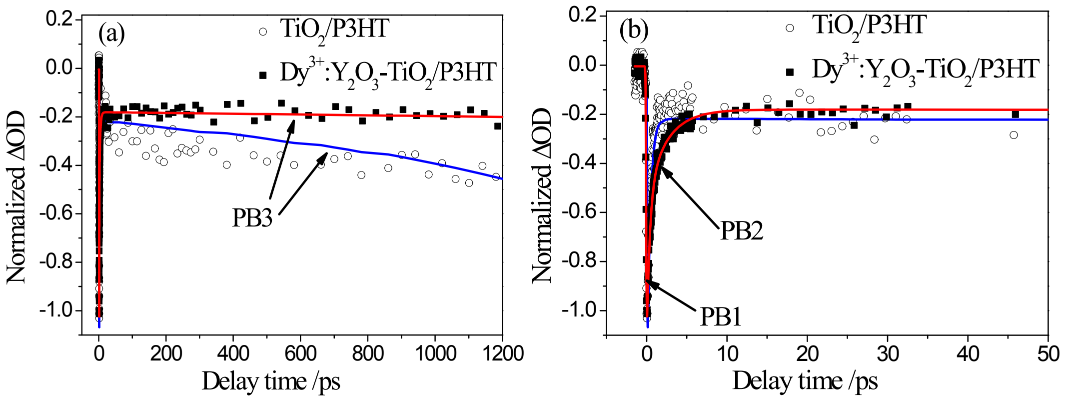

Fig. 4. (a)Normalized femtosecond transient absorption decays of TiO_2/P3HT (○) and Dy^{3+}:Y_2O_3 doped TiO_2/P3HT (■) films excited at 400 nm (100 μJ cm^{-2}) probed at 602 nm. Solid lines are fitting curves with exponential components. (b)The early time dynamics probed at 602 nm.

Table 1. Lifetimes and the amplitudes from fits to transient absorption decays using the linear superposition of electronic contributions described in the text.

lifetime(τ) (amplitude)	τ_{vib1} / ps (A)	$\tau_{hot\text{-}e}$ / ps (B)	τ_{re} / ns (C)	τ_{vib2} / ps (D)	$\tau_{complex}$ / ns (E)	τ_h / ns
Dy^{3+}:Y_2O_3-TiO_2/P3HT	0.70±0.01 (0.96)	25.1±0.8 (0.19)	0.7±0.2 (0.05)	0.39±0.04 (-0.91)	1.3±0.2 (-0.18)	1.26±0.19
Pure TiO_2/P3HT	0.75±0.01 (0.95)	30.2±1.0 (0.15)	14.0±1.5 (0.14)	0.80±0.04 (-0.81)	8.5±1.0 (-0.19)	6.94±0.67

Although the above analysis in sections 3.3 and 3.4 are based on one device only, nonetheless time-integrated PL measurements were provided to identify the charge transfer properties with selected electron/hole-only extraction layer, as shown in

Figure S6, which can further lend support to our work. Compared to TiO_2/P3HT, an efficient PL quenching for Dy^{3+}:Y_2O_3 -TiO_2/P3HT blend film can be ascribed to the redundant space provided or pores formed by the incorporation of Dy^{3+}:Y_2O_3 nanoparticles, thus favoring the physical adsorptions of P3HT molecules in virtue of intermolecular attractive forces.[53,54] As for the hole-only device P3HT/PEDOT:PSS, the emission intensity of P3HT was quenched intensely after coating on the hole extraction layer PEDOT:PSS. These high degrees of PL quenching indicate that the current configuration of Dy^{3+}:Y_2O_3-TiO_2/P3HT bears good electron and hole transport properties.

3.5. Photovoltaic characterizations of the HSCs

With a view to exploring the doping effect of Dy^{3+}:Y_2O_3 phosphors on the final photovoltaic performance, we prepared and characterized two types of films for comparison: pure TiO_2/P3HT and blended Dy^{3+}:Y_2O_3 doped TiO_2/P3HT films. The devices were fabricated by the sequential depositions of Dy^{3+}:Y_2O_3 doped TiO_2, P3HT, PEDOT:PSS and Pt electrode on a transparent FTO substrate. The morphology of Dy^{3+}:Y_2O_3 doped TiO_2 was characterized by SEM and TEM. It can be observed from Fig. 5a and Fig. 5c that the particle diameter of TiO_2 was estimated to be about 20~30 nm while the diameter of Y_2O_3 is much larger but still within nano-domain (about 100 nm). The surface of the TiO_2 layer clearly exhibits a porous structure, which benefits the improvement of p-n contact for BHJ[55-57]. On the other hand, the porous structure of TiO_2 layer is ready for the adsorption of P3HT molecules by trapping the solution in the microporomerics[58-60] in virtue of intermolecular attractive forces.[61-64] In addition, the cross-sectional SEM image of the photovoltaic layer was shown in Fig. 5b: the different layers and their individual thickness of the FTO, BHJ, and PEDOT:PSS can be clearly distinguished. Especially, the thickness of the photovoltaic layer was estimated to be about 200 nm as observed from Fig. 5b.

The photocurrent-voltage (*J*-*V*) characteristics and the photovoltaic performances of HSC with different loading amounts of $Dy^{3+}:Y_2O_3$ are shown in Fig.5f, and the photovoltaic parameters are summarized in Table 2. It reveals that with the increase of $Dy^{3+}:Y_2O_3$ amount in the HSCs from 0 wt% to 6 wt%, both V_{oc} and J_{sc} gradually increase. However, since when the amount of $Dy^{3+}:Y_2O_3$ exceeds 6.0 wt% in the doping layer, it is hard to form a flat film, thus a maximum conversion efficiency of 2.97% was achieved under the optimized loading amount of $Dy^{3+}:Y_2O_3$ phosphor at 6.0wt% in the doping layer. This can be further confirmed by IPCE measurements of solar cells made from different loading amounts of nanophosphors (Fig. 5e), which were carried out at given molar ratio of Dy^{3+} relative to Y_2O_3 at 5 mol% and exhibit the best IPCE at 6 wt% of $Dy^{3+}:Y_2O_3$. A slight but still appreciable increase of IPCE around 375 nm can be observed when the contents of $Dy^{3+}:Y_2O_3$ increases from 2wt% to 6wt%, which originates from the enhancement of down-conversion process by Dy^{3+}. Meanwhile, the broad IPCE covering the spectrum from 450 to 600 nm increases significantly with increasing the contents of $Dy^{3+}:Y_2O_3$, which we ascribe to the energy level tailoring effect as demonstrated in Fig. 5d. However, when the initial loading amount of $Dy^{3+}:Y_2O_3$ exceeds 6 wt%, it is hard to form a flat acceptor film, which can seriously influence the intimate contact between donor and acceptor, therefore, a notable decrease in IPCE (Fig. 5e) and device performance is observed.

Under the identical experimental conditions, the Dy^{3+}:Y_2O_3 doped TiO_2/P3HT HSC exhibit better device performances than the pure TiO_2/P3HT HSC of 2.02%. In detail, the photocurrent density J_{sc} has gradually increased from 6.10 to 7.89 mA·cm^{-2} while V_{oc} increases from 0.673 to 0.749 V, with the increase of the doping amounts of Dy^{3+}:Y_2O_3 phosphors from 0 wt% to 6 wt%. All these better performances can be ascribed to the energy level alignment induced by the incorporation of Dy^{3+}:Y_2O_3 and the resultant enhancements in light harvesting (*i.e.*, exciton generation), charge transfer and collection. The CB energy levels of TiO_2 at different doping concentrations of Dy^{3+}:Y_2O_3 nanophosphors were determined using Mott-Schottky plots. The Mott-Schottky results (Fig. 5d and Table S2) show that with the addition of Dy^{3+}:Y_2O_3, the CB energy levels of acceptor are substantially elevated from -4.19 to -3.77 eV. However, with further addition (exceeds 6 wt%) of the nanophosphors, the CB energy levels are affected little, down to -3.72 eV at 8 wt% from -3.77 eV at 6 wt%. It is worth mentioning that on one hand, Y_2O_3 plays the dominant role of tailoring energy level alignment since the concentration of Dy^{3+} is limited in view of the fact that the initial loading is small and there is also loss during the hydrothermal preparation; on the other hand, when the initial loading amount of Dy^{3+}:Y_2O_3 exceeds 6wt%, it is hard to form a flat acceptor film. Special attention was paid to the energy levels at the optimized doping concentration of 6 wt%: the CB and VB energy levels of acceptor are elevated by 0.57 and 0.32 eV, respectively, according to the CV characteristics and UV-vis spectrum (Supporting Information, Table S1). According to the relationship in Eq. (S3),[65] the elevated CB energy levels of acceptor with increasing the doping amount of Dy^{3+}:Y_2O_3 phosphors as demonstrated in the Mott-Shottcky in Fig. 5d and Table S2 can provide some insight into the slightly increased V_{OC} (from 0.673 to 0.749 V). The elevated CB energy levels simultaneously reduce the energy offset between the CB energy level of acceptor and LUMO energy level of donor, thus leading to enhanced electron transfer, which can interpret the increased short-circuit current density J_{SC} from as it is related to the charge separation and transfer. This demonstrates that the doping of lanthanide phosphors indeed is critical to the photovoltaic performance of solar cells. This work is initially motivated by exploring the potential powerful role of Dy^{3+}:Y_2O_3 playing in inorganic/organic HSCs through a simple architecture. However, having a better understanding of the underlying photophysical mechanism will shed some insight on the designing rule of optimizing photovoltaic devices in future.

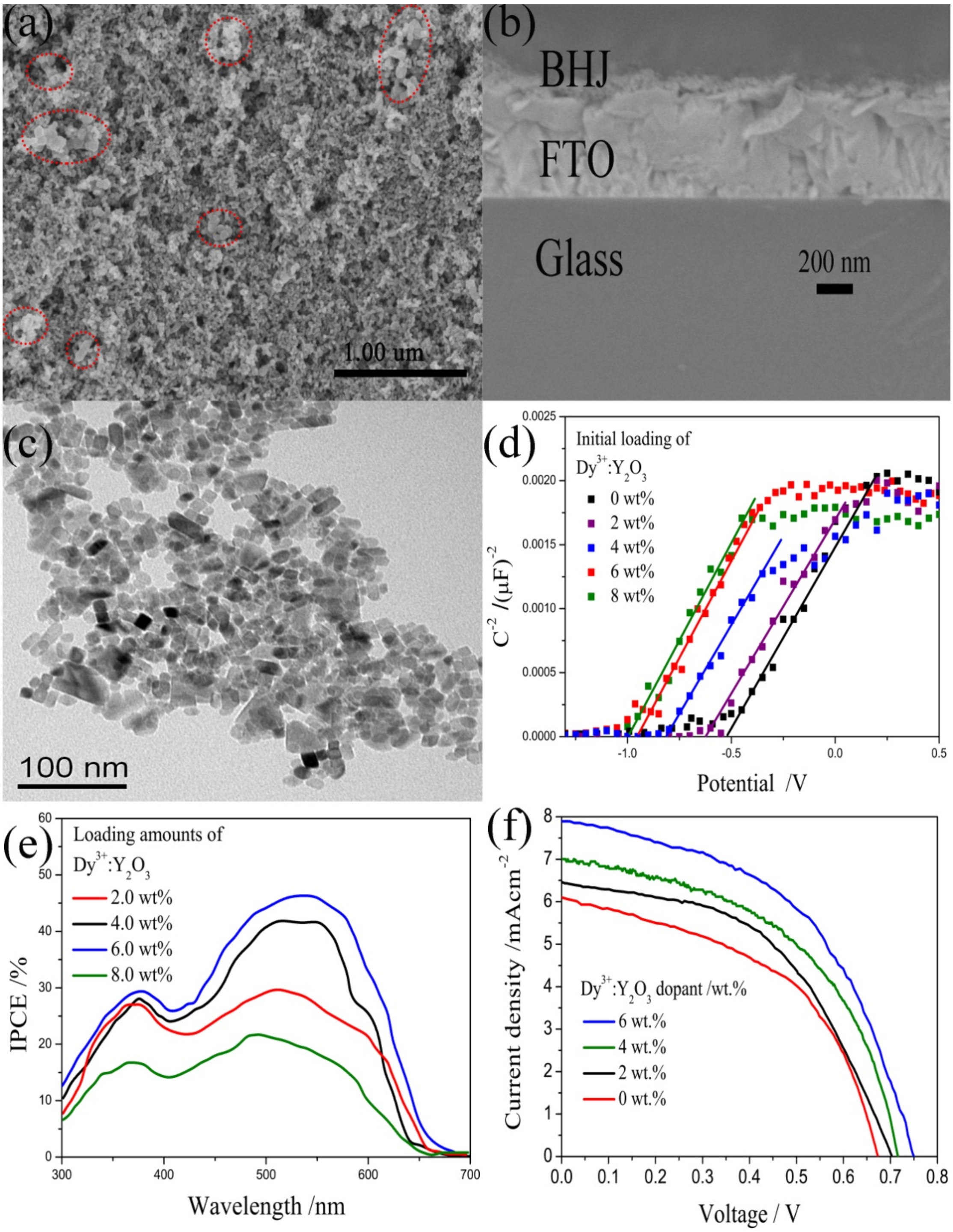

Fig. 5. Planar (a), cross-sectional (b) SEM images and TEM image (c) of the Dy^{3+}:Y_2O_3-TiO_2 acceptor layer, Mott-Schottky plots of the different films (d), IPCE and photocurrent-voltage (J-V) characteristics of HSCs made from different BHJs with different doping amount of Dy^{3+}:Y_2O_3 nanophosphor.

Table 2. Photovoltaic parameters of HSCs based on different bulk heterojunctions.

Dy^{3+}:Y_2O_3 dopant (wt%)	V_{oc} (mV)	J_{sc} (mA·cm^{-2})	*FF*	η^a (%)
0.0wt%.	673	6.10	0.49	2.02
2.0 wt%	703	6.43	0.50	2.30
4.0 wt%	716	7.00	0.50	2.52
6.0wt%	749	7.89	0.50	2.97

[a] $\eta = J_{sc} V_{oc} FF / P_{in}$, where P_{in} =100 mw·cm^{-2} (AM 1.5).

4. Conclusions

In summary, we have demonstrated that energy level alignment of TiO_2/P3HT systems was successfully tailored. That is, the CB and VB edges of acceptor were elevated by 0.57 and 0.32 eV, respectively with the doping concentration of Dy^{3+}:Y_2O_3 phosphors at 6 wt%. The results show that both the charge transports (including electron and hole) and the device performances have been significantly enhanced by Dy^{3+}:Y_2O_3 phosphors. Notably, the electron and hole transfer lifetimes have been shortened from 30.2 ps and 6.94 ns to 25.1 ps and 1.26 ns, respectively. And an efficiency of approaching 3% was achieved as compared with the pure TiO2, which can be ascribed to the widened absorption range of P3HT except the tailored energy level induced by rare-earth phosphors. This work underscores the potentials of rare-earth phosphors in pursing highly efficient optoelectronic devices with excellent charge-transport properties by tuning appropriate energy level configurations.

Acknowledgements

The authors gratefully acknowledge the financial support of the Natural Science

Foundation of China (61366003), the science and technology project of the education department of Jiangxi Province, China (GJJ12449, GJJ12455, GJJ14533), Aviation Science Fund of China (2013ZF56025).

References

1 H.-P. Wang, T.-Y. Lin, C.-W. Hsu, M.-L. Tsai, C.-H. Huang, W.-R. Wei, M.-Y. Huang, Y.-J. Chien, P.-C. Yang, C.-W. Liu, L.-J. Chou and J.-H. He, *ACS NAno*, **2013**, *7*, 9325-9335.

2 J. H. Noh, S. H. Im, J. H. Heo, T. N. Mandal and S. I. Seok, *Nano Lett.*, **2013**, *13*, 1764-1769.

3 A. Abrusci, S. D. Stranks, P. Docampo, H.-L. Yip, A. K. Y. Jen and H. J. Snaith, *Nano Lett.*, **2013**, *13*, 3124-3128.

4 P. Maraghechi, A. J. Labelle, A. R. Kirmani, X. Lan, M. M. Adachi, S. M. Thon, S. Hoogland, A. Lee, Z. Ning, A. Fischer, A. Amassian and E. H. Sargent, *ACS Nano*, **2013**, *7*, 6111-6116.

5 F. Gao, S. Ren and J. Wang, *Energy Environ. Sci.*, **2013**, *6*, 2020-2040.

6 H. Chen, X. Pan, W. Liu, M. Cai, D. Kou, Z. Huo, X. Fang and S. Dai, *Chem. Commun.*, **2013**, *49*, 7277-7279.

7 B. Cai, Y. Xing, Z. Yang, W.-H. Zhang and J. Qiu, *Energy Enviorn. Sci.*, **2013**, *6*, 1480-1485.

8 X. Jin, W. F. Sun, Z. H. Chen, Y. Li, P. J. Li, X. D. He, Y. B. Yuan, S. B. Zou, Y. C. Qin and Q. H. Li, *J. Power Sources*, **2014**, *268*, 874-881.

9 Q. H. Li, Y. B. Yuan, Z. H. Chen, T. H. Wei, X. Jin, Y. Li, S. B. Zou and W. F.

Sun, *ACS Appl. Mater. Interfaces*, **2014**, *6*, 12798-12807.

10 Q. H. Li, Y. B. Yuan, T. H. Wei, Y. Li, Z. H. Chen, X. Jin, Y. C. Qin and W. F. Sun, *Sol. Energy Mater. Sol. Cells*, **2014**, *130*, 426-434.

11 S. Shoaee, J. Briscoe, J. R. Durrant and S. Dunn, *Adv. Mater.*, **2014**, *26*, 263-268.

12 J. Lee, S. Mubeen, G. Hernandez-Sosa, Y. Sun, F. M. Toma, G. D. Stucky and M. Moskovits, *Adv. Mater.*, **2013**, *25*, 256-260.

13 X. Wang, T. Ishwara, W. Gong, M. Campoy-Quiles, J. Nelson and D. D. C. Bradley, *Adv. Funct. Mater.*, **2012**, *22*, 1454-1460.

14 Y. He, H. Y. Chen, J. Hou and Y. Li, **2010**, *132*, 1377-1382.

15 S. Liao, H. Jhuo, Y. S. Cheng and S. A. Chen, *Adv. Mater.*, **2013**, *25*, 4766-4771.

16 S. Ren, L.-Y. Chang, S.-K. Lim, J. Zhao, M. Smith, N. Zhao, V. Bulović, M. Bawendi and S. Gradečak, *Nano Lett.*, **2011**, *11*, 3998-4002.

17 H. Ohkita and S. Ito, *Polymer*, **2011**, *52*, 4397-4417.

18 M. Granstrom, K. Petritsch, A. C. Arias, A. Lux, M. R. Andersson and R. H. Friend, *Nature*, **1998**, *395*, 257-260.

19 W. U. Huynh, J. J. Dittmer and A. P. Alivisatos, *Science*, **2002**, *295*, 2425-2427.

20 B. Yang, Y. Yuan, P. Sharma, S. Poddar, R. Korlacki, S. Ducharme, A. Gruverman, R. Saraf and J. Huang, *Adv. Mater.*, **2012**, *24*, 1455-1460.

21 B. Rand, D. Burk and S. Forrest, *Phys. Rev. B*, **2007**, *75*, 115327.

22 X. Gong, M. Tong, F. G. Brunetti, J. Seo, Y. Sun, D. Moses, F. Wudl and A. J. Heeger, *Adv. Mater.*, **2011**, *23*, 2272-2277.

23 Z. Gu, L. Yan, G. Tian, S. Li, Z. Chai and Y. Zhao, *Adv. Mater.*, **2013**, *25*, 3758-3779.

24 J. Zhou, Z. Liu and F. Li, *Chem. Soc. Rev.*, **2012**, *41*, 1323-1349.

25 J. Wang, J. Wu, J. Lin, M. Huang, Y. Huang, Z. Lan, Y. Xiao, G. Yue, S. Yin and T. Sato, *ChemSusChem*, **2012**, *5*, 1307-1312.

26 J. Wu, J. Wang, J. Lin, Z. Lan, Q. Tang, M. Huang, Y. Huang, L. Fan, Q. Li and Z. Tang, *Adv. Energy Mater.*, **2012**, *2*, 78-81.

27 L. D. Carlos, R. A. Ferreira, V. de Zea Bermudez, B. Julián-López and P. Escribano, *Chem. Soc. Rev.*, **2011**, *40*, 536-549.

28 M. Haase and H. Schafer, *Angewandte Chemie*, **2011**, *50*, 5808-29.

29 Z. Gu, L. Yan, G. Tian, S. Li, Z. Chai and Y. Zhao, *Advanced materials*, **2013**, *25*, 3758-79.

30 F. Wang, R. Deng, J. Wang, Q. Wang, Y. Han, H. Zhu, X. Chen and X. Liu, *Nat. Mater.*, **2011**, *10*, 968-973.

31 K. Takaichi, H. Yagi, J. Lu, J. F. Bisson, A. Shirakawa, K. Ueda, T. Yanagitani and A. A. Kaminskii, *Appl. Phys. Lett.*, **2004**, *84*, 317.

32 G. Yang, S. Zhou, H. Lin and H. Teng, *Physica B*, **2011**, *406*, 3588-3591.

33 H. Guo and S. Sun, *Nanoscale*, **2012**, *4*, 6692-6706.

34 H. Hoda, W. Jihuai, L. Zhang, L. Qinghua, X. Guixiang, L. Jianming, H. Miaoliang, H. Yunfang and M. S. Abdel-Mottaleb, *Nanotechnology*, **2010**, *21*,

415201.

35 J.-X. Zhao, X.-H. Lu, Y.-Z. Zheng, S.-Q. Bi, X. Tao, J.-F. Chen and W. Zhou, *Electrochem. Commun.*, **2013**, *32*, 14-17.

36 J. Wu, J. Wang, J. Lin, Y. Xiao, G. Yue, M. Huang, Z. Lan, Y. Huang, L. Fan, S. Yin and T. Sato, *Sci. Rep.*, **2013**, *3*, 2058.

37 J. Wu, S. Hao, Z. Lan, J. Lin, M. Huang, Y. Huang, P. Li, S. Yin and T. Sato, *J. Am. Chem. Soc.*, **2008**, *130*, 11568-11569.

38 J. Wu, S. Hao, J. Lin, M. Huang, Y. Huang, Z. Lan and P. Li, *Cryst. Growth Des.*, **2007**, *8*, 247-252.

39 Q. Li, J. Wu, Q. Tang, Z. Lan, P. Li, J. Lin and L. Fan, *Electrochem. Commun.*, **2008**, *10*, 1299-1302.

40 T. M. Clarke and J. R. Durrant, *Chem. Rev.*, **2010**, *110*, 6736-6767.

41 S. D. Stranks, G. E. Eperon, G. Grancini, C. Menelaou, M. J. Alcocer, T. Leijtens, L. M. Herz, A. Petrozza and H. J. Snaith, *Science*, **2013**, *342*, 341-344.

42 M. Liu, M. B. Johnston and H. J. Snaith, *Nature*, **2013**, *501*, 395-398.

43 J. M. Lee, B. H. Kwon, H. I. Park, H. Kim, M. G. Kim, J. S. Park, E. S. Kim, S. Yoo, D. Y. Jeon and S. O. Kim, *Adv. Mater.*, **2013**, *25*, 2011-2017.

44 D. Cheyns, J. Poortmans, P. Heremans, C. Deibel, S. Verlaak, B. Rand and J. Genoe, *Phys. Rev. B*, **2008**, *77*, 165332.

45 A. A. Bakulin, J. C. Hummelen, M. S. Pshenichnikov and P. H. Van Loosdrecht, *Adv. Funct. Mater.*, **2010**, *20*, 1653-1660.

46 V. I. Klimov, *Annu. Rev. Phys. Chem.*, **2007**, *58*, 635-673.

47 D. McMorrow, W. T. Lotshaw and G. A. Kenneywallace, *IEEE J. Quantum Electron.*, **1988**, *24*, 443-454.

48 A. Kongkanand, K. Tvrdy, K. Takechi, M. Kuno and P. Kamat, *J. Am. Chem. Soc.*, **2008**, *130*, 4007-4015.

49 Z. Pan, H. Zhang, K. Cheng, Y. Hou, J. Hua and X. Zhong, **2012**, *6*, 3982-3991.

50 Z. Pan, I. M. Sero, Q. Shen, H. Zhang, Y. Li, K. Zhao, J. Wang, X. Zhong and J. Bisquert, *J. Am. Chem. Soc.*, **2014**, *136*, 9203-9210.

51 G. Xing, N. Mathews, S. Sun, S. S. Lim, Y. M. Lam, M. Gratzel, S. Mhaisalkar and T. C. Sum, *Science*, **2013**, *342*, 344-347.

52 X. Jin, W. Sun, Z. Chen, T. Wei, C. Chen, X. He, Y. Yuan, Y. Li and Q. Li, *ACS Appl. Mater. Interfaces*, **2014**.

53 W. F. Sun, Q. H. Zeng and A. B. Yu, *Langmuir*, **2013**, *29*, 2175-2184.

54 W. F. Sun, Q. H. Zeng, A. B. Yu and K. Kendall, *Langmuir*, **2013**, *29*, 7825-7837.

55 S. Shoaee, J. Briscoe, J. R. Durrant and S. Dunn, *Adv. Mater.*, **2014**, *26*, 263-268.

56 G. Xing, N. Mathews, S. Sun, S. S. Lim, Y. M. Lam, M. Grätzel, S. Mhaisalkar and T. C. Sum, *Science*, **2013**, *342*, 344-347.

57 J. Burschka, N. Pellet, S.-J. Moon, R. Humphry-Baker, P. Gao, M. K. Nazeeruddin and M. Grätzel, *Nature*, **2013**, *499*, 316-319.

58 A. Hagfeldt, S.-E. Lindquist and M. Grätzel, *Sol. Energ. Mater. Sol. Cells*, **1994**, *32*, 245-257.

59 B. He, X. Meng and Q. Tang, *ACS Appl. Mater. Inter.*, **2014**, *6*, 4812-4818.

60 B. He, X. Meng, Q. Tang, P. Li, S. Yuan and P. Yang, *J. Power Sources*, **2014**, *260*, 180-185.

61 W. F. Sun, *Nanoscale*, **2013**, *5*, 12658-12669.

62 W. F. Sun, *Phys. Chem. Chem. Phys.*, **2014**, *16*, 5846-5854.

63 W. F. Sun, Y. C. Li, W. Xu and Y. W. Mai, *RSC Adv.*, **2014**, *4*, 34500-34509.

64 W. F. Sun, Q. H. Zeng and A. B. Yu, *RSC Adv.*, **2014**, *4*, 38505-38516.

65 R. Kroon, M. Lenes, J. C. Hummelen, P. W. M. Blom and B. de Boer, *Polym. Rev.*, **2008**, *48*, 531-582.

Captions for Figures and Tables

Fig. 1. (a) XRD patterns of bare TiO_2, dysprosium ion decorated yttrium oxide (Dy^{3+}:Y_2O_3) and Dy^{3+}:Y_2O_3-doped TiO_2; (b) TEM images of the prepared Dy^{3+}:Y_2O_3; (c) and (d) HR-TEM images showing an individual nanocrystal of Dy^{3+}:Y_2O_3 and the insets are the corresponding SAED patterns.

Fig. 2. Energy level diagram of acceptor/donor showing optical excitation (up arrow), nonradiative relaxation (curved line), radiative relaxation (down arrow) and the electron and hole transfer times at the either Dy^{3+}:Y_2O_3 doped TiO_2/P3HT or TiO_2/P3HT interfaces. $\left|n\right\rangle$ refers to the vibrational eigenstates involved in the transitions. The VB and CB energy levels of pure TiO_2 are also shown for comparison. The LUMO and HOMO of P3HT are -3.0 and -5.1 eV, respectively.

Fig. 3. (a) Normalized femtosecond transient absorption decays of Dy^{3+}:Y_2O_3 doped TiO_2/P3HT (○) and pure TiO_2/P3HT (■) films excited at 400 nm (100 μJ cm^{-2}) probed at 650 nm. Solid lines are fitting curves with exponential components. (b) The early time dynamics probed at 650 nm.

Fig. 4. (a)Normalized femtosecond transient absorption decays of TiO_2/P3HT (○) and Dy^{3+}:Y_2O_3 doped TiO_2/P3HT (■) films excited at 400 nm (100 μJ cm^{-2}) probed at 602 nm. Solid lines are fitting curves with exponential components. (b)The early time dynamics probed at 602 nm.

Fig. 5. Planar (a), cross-sectional (b) SEM images and TEM image (c) of the Dy^{3+}:Y_2O_3-TiO_2 acceptor layer, Mott-Schottky plots of the different films (d), IPCE and photocurrent-voltage (J-V) characteristics of HSCs made from different BHJs with different doping amount of Dy^{3+}:Y_2O_3 nanophosphor.

Table 1. Lifetimes and the amplitudes from fits to transient absorption decays using the linear superposition of electronic contributions described in the text.

Table 2. Photovoltaic parameters of HSCs based on different bulk heterojunctions.